Predictive modeling of lung motion over the entire respiratory cycle using measured pressure-volume data, 4DCT images, and finite-element analysis

Jaesung Eom, Xie George Xu,[a] and Suvranu De[b]
Department of Mechanical, Aerospace and Nuclear Engineering, Rensselaer Polytechnic Institute, Troy, New York 12180

Chengyu Shi
Department of Radiation Oncology, University of Texas Health Science Center at San Antonio, San Antonio, Texas 78229

(Received 20 October 2009; revised 25 May 2010; accepted for publication 27 May 2010; published 28 July 2010)

Purpose: Predicting complex patterns of respiration can benefit the management of the respiratory motion for radiation therapy of lung cancer. The purpose of the present work was to develop a patient-specific, physiologically relevant respiratory motion model which is capable of predicting lung tumor motion over a complete normal breathing cycle.
Methods: Currently employed techniques for generating the lung geometry from four-dimensional computed tomography data tend to lose details of mesh topology due to excessive surface smoothening. Some of the existing models apply displacement boundary conditions instead of the intrapleural pressure as the actual motive force for respiration, while others ignore the nonlinearity of lung tissues or the mechanics of pleural sliding. An intermediate nonuniform rational basis spline surface representation is used to avoid multiple geometric smoothing procedures used in the computational mesh preparation. Measured chest pressure-volume relationships are used to simulate pressure loading on the surface of the model for a given lung volume, as in actual breathing. A hyperelastic model, developed from experimental observations, has been used to model the lung tissue material. Pleural sliding on the inside of the ribcage has also been considered.
Results: The finite-element model has been validated using landmarks from four patient CT data sets over 34 breathing phases. The average differences of end-inspiration in position between the landmarks and those predicted by the model are observed to be 0.450 ± 0.330 cm for Patient P1, 0.387 ± 0.169 cm for Patient P2, 0.319 ± 0.186 cm for Patient P3, and 0.204 ± 0.102 cm for Patient P4 in the magnitude of error vector, respectively. The average errors of prediction at landmarks over multiple breathing phases in superior-inferior direction are less than 3 mm.
Conclusions: The prediction capability of pressure-volume curve driven nonlinear finite-element model is consistent over the entire breathing cycle. The biomechanical parameters in the model are physiologically measurable, so that the results can be extended to other patients and additional neighboring organs affected by respiratory motion. [DOI: 10.1118/1.3455276]

Key words: 4DCT, FEM, NURBS surface reconstruction, respiratory motion, lung model

I. INTRODUCTION

In external beam radiation treatment, the goal to deliver a lethal radiation dose through external beams conformed to the tumor while sparing adjacent healthy tissues may be compromised by organ motions.[1–12] The current radiation treatment paradigm, for the most part, is still based on an assumption that both the tumor location and shape are known and remain unchanged during the course of radiation delivery. This assumption fails in anatomical sites such as the thoracic cavity and the abdomen, owing predominantly to respiratory motions.[2–6] In the lungs, for example, respiration related deformation[13] can be as much as 4 cm. As a result, although higher radiation doses have shown better local tumor control, less aggressive treatment strategies with various degrees of dose margin have been adopted to accommodate for potential targeting errors.[14–17] Based on four-dimensional computed tomography (4DCT),[18–23] the motion margin can be estimated more accurately by overlapping information from all the phases. However, patient breathing pattern changes from time to time; the estimated margin from 4DCT may not represent the real margin for the delivery. Modeling of respiratory motion presents a unique multidisciplinary challenge. Although such research was reported as early as the 1940s,[24] dynamic modeling was not considered owing to past limitations in computer and medical imaging technologies. The challenge is especially interesting in the context of biomechanical modeling because the lung motion has uniquely complex spatial and temporal patterns. In space, the different lung lobes have varying ranges of deformation.[3,6,7] In time, the respiratory cycle can be unstable and patient dependent.[25,26] To predict the lung motion, one must take

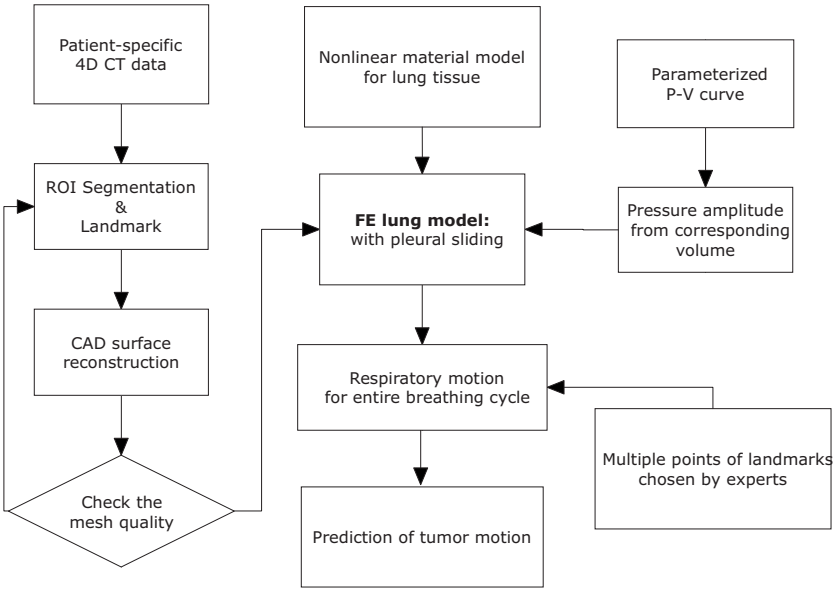

FIG. 1. A flow diagram of the modeling scheme showing the steps to convert 4DCT images to FE models with boundary conditions.

into account of nonlinear elasticity of lung tissue,[27,28] pleural sliding,[29,30] regional differences in lung response, and the motion of adjacent structures such as the heart.[31,32]

Although deformable image registration models[33] and nonmodel heuristic approaches[25] incorporating surrogates have provided information on tumor displacement caused by respiration, advanced finite-element methods (FEMs) can address limitations associated with these methods, including prediction of localized deformation of tumor[34] and interorgan interactions such as the pleural sliding.[35] Finite-element lung models have also been used to evaluate the effect of gravity on respiratory physiology[36] and to find surface matching of organs in two images in deformable image registration techniques.[37–40] Recently, finite-element lung models for tumor tracking at the end of inhalation incorporating contact conditions have been proposed.[35,34] In FEM, the effectiveness of the model and its accuracy in predicting tumor motion depend on several important issues including the quality of the patient geometric model and the regularity and accuracy of the finite-element mesh. In previous works by Brock *et al.*,[38] Werner *et al.*,[34] and Villard *et al.*,[41] multistep procedures such as isosurface construction, multiple iterative mesh smoothing, relaxing, and decimation may result in undue simplification and artifacts in the modeling as pointed out in Sec. III A of this paper. Additionally, the idea of using a projected displacement boundary condition by Brock *et al.*[38] and Al-Mayah *et al.*[35,42] on the surface of the lungs may misrepresent the physiology and incorrectly represent contact conditions with adjacent tissues.

The biomechanical engineering community has been studying the deformation mechanics of the lungs for many years. The first continuum-based FE model of a dome shaped lung was proposed by West and Matthews[43] in 1972. Linear and nonlinear elastic material models, obtained from experiments by Radford[44] on strips of tissue excised from canine lungs, were used in the model. Zhang *et al.*[37] proposed a lung model with pleural sliding which was driven by pressure forces applied on the surface of the lungs. This model was implicitly validated by overlaying the CT lung image at inhalation and a reconstructed image of the lung at exhalation without quantitative comparisons. Villard *et al.*[40] described a 3D deformable continuum-based lung model with pleural sliding. They showed that the simulation of pleural sliding produce results which are in closer agreement with clinical

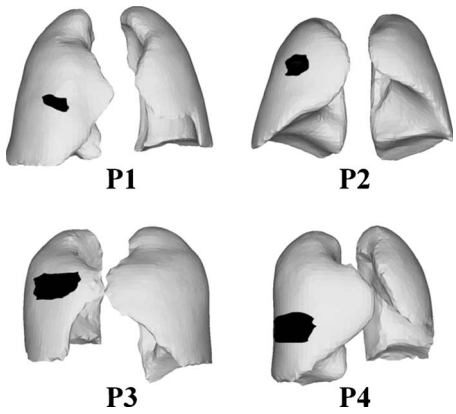

FIG. 2. Geometry and tumor location of all four patients (P1–P4).

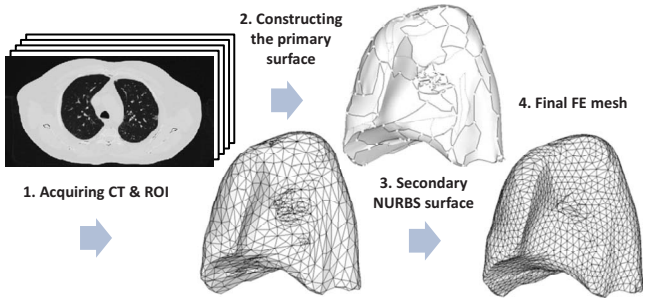

FIG. 3. Sequence of steps in converting 4DCT image data into a FE mesh through an intermediate NURBS representation in P2.

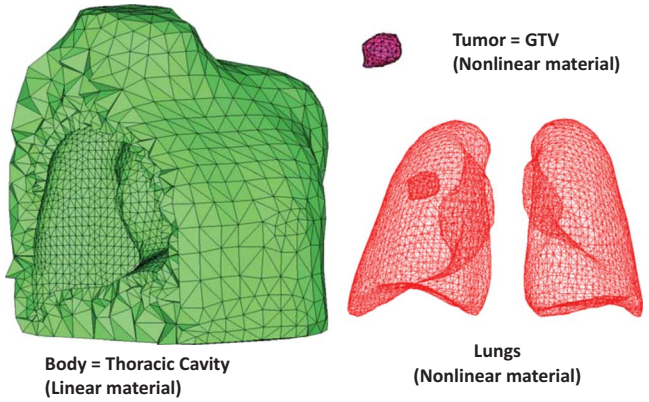

FIG. 4. FE models including a thoracic cavity, a tumor (gross target volume for radiation treatment purposes), and lungs for P2.

data. In an extension of this work, Didier *et al.*[39] used the same FEM model and investigated the kinematic effects of the ribs on the motion during a breathing cycle by using a finite helical axis (FHA) method. Extending the work of Zhang *et al.*,[37] Werner *et al.*[34,45] recently proposed a respiratory lung motion model incorporating contact mechanics. Instead of using contact elements, an augmented Lagrangian algorithm was used for the contact formulation in the FEM software COMSOL MULTIPHYSICS (COMSOL AB, Sweden). Brock *et al.*[38] developed a FE model driven by displacement fields obtained from CT images. This approach is capable of handling multiple organs. The initial and final states of the lungs and the other organs are obtained from the CT scans from the end of expiration (EE) and end of inspiration (EI), respectively. None of these FEM models discussed above considered the nonlinear elastic property associated with lung motion. Recently, Al-Mayah *et al.*[35,42] has improved the FEM-based 3D lung model in Brock *et al.*[38] by including contact conditions and nonlinear material properties. Prescribed displacement boundary conditions, similar to that in Brock *et al.*,[38] have been applied and the interaction between the walls of the lungs and the chest has been modeled using frictionless surface-based elements. However, the lung motion in their study was simulated using displacement boundary conditions which are not physiologically relevant.[36]

Although the previous studies offer insights into continuum-based lung modeling, none has presented results of tumor tracking over the entire breathing cycle as these studies lack one or more of the following three key features: Physiologically correct boundary conditions, physically realistic contact-friction modeling of pleural sliding, and empirically derived nonlinear mechanical properties of lung tissue. The necessity of including all three features is dictated by the mechanics of lung motion and the biomechanics of the lung tissue as explained in Sec. II B.

In this paper, we present a physics-based modeling

TABLE I. Summary of our nonlinear FE lung model (see Video 1[URL: http://dx.doi.org/10.1118/1.3455276.1]).

	Features
Geometric model	ROIs of multiple consistent breathing phase of 4 patients
FE mesh	Four-noded linear tetrahedral elements (C3D4) in ABAQUS/Standard[a]
Material properties	Lung tissue:[b] Homogeneous isotropic, hyperelastic model with strain energy per unit volume ($\rho_0 W$), $\rho_0 W = \frac{1}{2}c\exp(a_1E_{xx}^2+a_2E_{yy}^2+2a_4E_{xx}E_{yy})+\frac{1}{2}c\exp(a_1E_{xx}^2+a_2E_{zz}^2+2a_4E_{xx}E_{zz})+\frac{1}{2}c\exp(a_1E_{zz}^2+a_2E_{yy}^2+2a_4E_{zz}E_{yy})$, where $c=11.8$ g/cm, $a_1=0.43$, $a_2=0.56$, $a_4=0.32$, and E_{xx}, E_{xy} etc., are the components of the Green strain
	Ribcage:[c] Homogeneous isotropic, elastic model
	Young's modulus (E)=6.0 kPa, Poisson's ratio (ν)=0.4
Contact model	Augmented Lagrange multiplier with artificial damping for stabilization
	Surface based master-slave frictionless contact condition:[d,e] Visceral pleural surface (lung side) as slave and parietal pleural surface (ribcage side) as master surface
Load and boundary conditions	Uniform intrapleural pressure assumption[e,f] over the lung surface: Pressure amplitude history from computed volumes of 4DCT at multiple breathing phases and parameterized P-V curve data.[g] Fixed displacement boundary condition at root of lung[e] (trachea-lung junction chosen from CT)

[a]Reference 54.
[b]Reference 55.
[c]Reference 38.
[d]Reference 29.
[e]Reference 51.
[f]Reference 50.
[g]Reference 52.

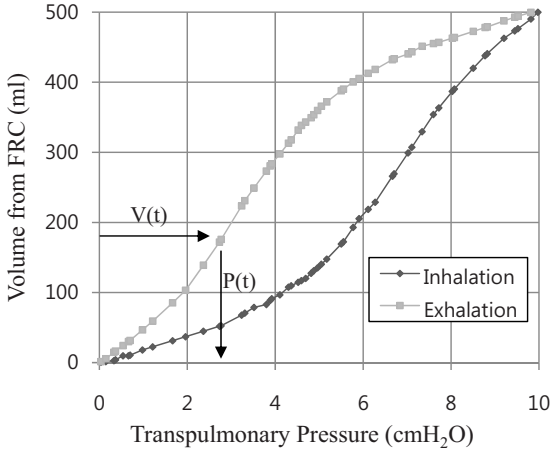

FIG. 5. Pressure-volume relationship from the parameterized P-V curve (Ref. 52) (TV=500 ml and transpulmonary pressure=10 cm H_2O).

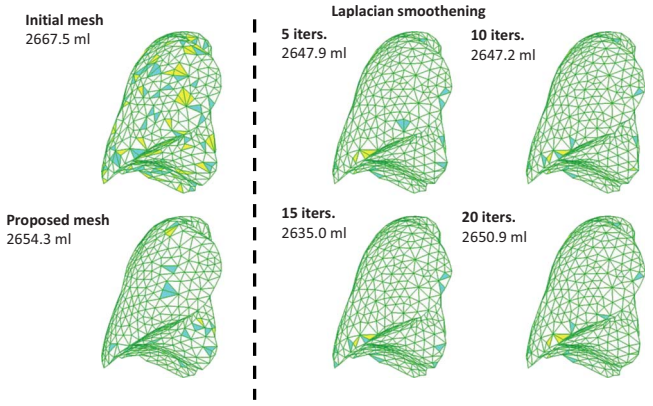

FIG. 6. Comparison of relaxing (Laplacian smoothing) vs proposed NURBS surface reconstruction procedure in P2 showing changes in mesh volume and elements that are close to or violating the quality indices.

method of respiratory motion that was based on 4DCT data of four patients. An intermediate nonunifrom rational B-spline (NURBS) surface representation was used to avoid multiple geometric smoothing procedures employed in previous work.[34,38,46] A nonlinear hyperelastic material model is used together with physiologically relevant boundary conditions based on pressure-volume (P-V) curves and pleural sliding. The FE model has been validated using 48 landmarks from the CT data. No tuning of FE modeling parameters including material properties,[34] contact stiffness,[37] or friction coefficients[42] was employed. In II, we present our modeling methodology, followed by a discussion of results in Sec. III and conclusions in Sec. IV.

II. METHODS AND MATERIALS

A flow diagram of our modeling scheme is presented in Fig. 1 which shows the procedure for creating the geometric model from patient-specific 4DCT data (Sec. II A) and our technique of physiologically based lung motion modeling (Sec. II B)

II.A. Patient specified geometric modeling

The first step in respiratory motion modeling is to develop FE models of the lungs and associated structures from 4DCT data. As shown in Fig. 2, four patient 4DCT data set were used; one was publicly available 4D respiratory-gated CT image data set, a point-validated pixel-based breathing thorax model,[47] and the other three were acquired at the center of collaborator. Each image slice has a resolution of 0.98 $\times 0.98$ mm^2 with a slice thickness of 2 mm, resulting in a $512 \times 512 \times 141$ voxel matrix. For each patient data set, ten breathing phases in the 4DCT DICOM data were segmented[48] into different regions of interest (ROIs) using the Pinnacle system (Version 8.0 m, Medical systems, Milpitas, CA).

According to the computed lung volume of each phase, the EE state, the EI state, and states in between were selected for modeling. The ROIs at the EE from this procedure are used as lung geometry (inner pleural surface) and the ROIs at the EI are used as ribcage (outer pleural surface). Though image data set were captured along breathing signal, real-time position management system (Varian Medical System, Palo Alto, CA), the volume of corresponding phases were used to sort the actual order of breathing phases. The volume change over time is monotonic function during either inhalation or exhalation; this means that the volume of lungs only increases during inhalation and decrease during exhalation. For example, Patient P1 has originally ten 4DCT phases per each patient data set. But two inconsistent breathing phases which have increasing volume exist during exhalation. So

TABLE II. Comparison of mesh quality indices in the percentage of elements violating threshold criteria.

Mesh	Jacobian (<0.9)	Aspect ratio (>2.0)	Maximum angle (>80°)	Minimum angle (<50°)
Initial	21.1%	0.2%	49.9%	83.7%
		Laplacian smoothing		
Five iterations	4.2%	0.2%	28.3%	66.9%
Ten iterations	4.1%	0.2%	27.7%	66.0%
15 iterations	3.4%	0.2%	24.7%	63.7%
20 iterations	3.9%	0.2%	27.6%	66.2%
Proposed model	3.0%	0.0%	21.3%	59.3%

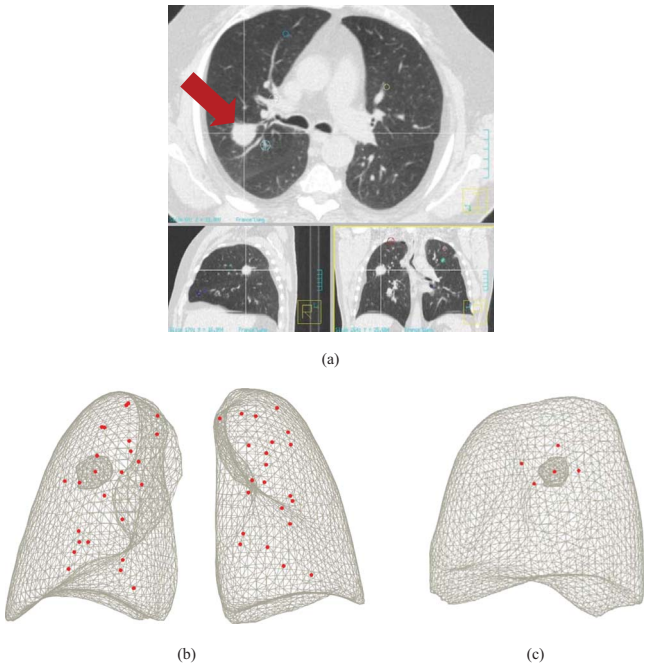

FIG. 7. Landmark positions of P2; bifurcation of vessels and airway were determined by radiologists (a) locating landmarks at anatomical points of bifurcations and at the center of the tumor (tumor, arrow; LR-AP, sectional view on top; AP-SI, sectional view on bottom left; LR-SI, sectional view on bottom right); (b) 48 points of landmarks; and (c) five points of landmarks close to the tumor.

these two inconsistent breathing phases are excluded in the modeling. The finally chosen breathing phase of each patient are presented in Sec. III D.

For accurate simulations, a uniform "good quality" mesh with elements that have small aspect ratios and include angles must be used.[49] However, mesh models generated from patient-specific CT images tend to have a dense arrangement of elements with highly irregular geometries, which cannot be directly used for FE analysis. In previous studies,[34,38,41] multiple iterations[38] of mesh decimation and Laplacian smoothing were used to reduce the number of elements and generate a more uniform mesh acceptable in FE simulations. The problem of this procedure is that the detail of the mesh topology may be lost since Laplacian smoothing focuses on moving point locations to improve triangulation while neglecting the preservation of the original geometric features. Also, the procedure is not interactive as multiple steps are involved. In this study, we have used a NURBS surface reconstruction approach to convert the ROIs into FE meshes as shown in Fig. 3. Primary surfaces are generated from ROI contour lines in Rhinoceros 3D (Robert McNeel & Associates, Seattle, WA). NURBS surfaces were then reconstructed and converted into suitable FE meshes using HYPERMESH (Altair Engineering, Troy, MI). This approach greatly simplified the procedure of FE mesh generation from CT scanned image data without losing the geometric details. In Sec. III, we will compare the NURBS surface reconstruction technique with Laplacian smoothing. The each FE model is composed of the thoracic cavity and the lungs with an embedded tumor in the right lung as seen in Fig. 4.

II.B. Physiological respiratory motion modeling

In this work we have developed a physics-based lung model using FEM, which takes into account the physiology of respiratory motion, the biomechanics of the lung tissue, and the sliding of the lungs on the inside of the ribcage. Since the lung itself is a passive organ, its deformation is driven primarily by the intrapleural pressure changes caused by relative motion of other anatomical structures such as the ribcage and the diaphragm.[36] So-called "P-V" curves[50,51] are plotted to represent the relationship between the lung volume (V) and transmural pressure (P) changes. We have used the P-V data to apply pressure boundary conditions to the surface of the lung model based on its instantaneous volume so that the relationship between lung volume and pressure is maintained. We believe that this is an advantage of our modeling approach compared to models that apply displacement boundary conditions[35,38] to drive lung motion.

The features of our FE model are summarized in Table I. A distributed time-varying pressure load was applied to the surface of the FE lung model. Pressure amplitudes at each breathing phase were evaluated from the parametrized P-V curve[52] and the mean P-V curve[53] shown in Fig. 5. The *in situ* lung volumes over multiple breathing phases were computed from the segmented 4DCT data between the EE and the EI and the volume difference at corresponding breathing phases lead the corresponding pressure, which was read off from the P-V curve. Though in Fig. 5, the value of volume of tidal volume (TV) and pressure was used as 500 ml and 10 cm H_2O for illustration, the pressures at EI are evaluated by the mean P-V curve[53] and the change of scaled pressure over volume are fitted by the parameterized P-V curve.[52]

A tumor-bearing lung is modeled as an elastic medium Ω consisting of N homogeneous isotropic subdomains in the finite-element model of ABAQUS. The external surface of lung $\partial\Omega$ is decomposed in $\partial\Omega_d$, where the displacements $\hat{\mathbf{u}}$ are prescribed by the anatomical facts (root of lung), and $\partial\Omega_t$

TABLE III. Characteristics of the finite-element model of each patient.

Name	Number of phases	Total landmarks	Avg. volume of tetrahedral (ml)	Node/elements	Computation time
P 1	8	48	0.111	7274/30 320	1 hr 30 min
P 2	8	48	0.165	6184/25 212	2 hr
P 3	10	46	0.081	5797/24 938	2 hr 45 min
P 4	8	39	0.101	7748/35 830	2 hr 20 min

TABLE IV. The different breathing phases are distinguished by volume change from EE (ml) and provided unique identifiers.

Breathing phase identifier	Volume change ($\mathbf{V}-\mathbf{V}_{EE}$) (ml)			
	P1	P2	P3	P4
EE	0	0	0	0
IN-1	43.47	189.16	5.59	68.6
IN-2	51.15	252.03	70.21	175.98
IN-3	⋯	412.67	273.13	⋯
IN-4	⋯	443.62	354.26	⋯
IN-5	⋯	⋯	403.51	⋯
EI	244.5	453.97	404.86	354.92
EX-1	243.58	303.41	301.52	354.02
EX-2	130.76	237.82	170.54	342.35
EX-3	60.47	⋯	55.2	69.6
EX-4	57.72	⋯	⋯	16.15

where distributed surface traction $\hat{\mathbf{t}}$ are applied. The locally uniform elastic regions $\Omega^I(I=1,\ldots,N)$ are implanted into the lung Ω. The boundary of local region Ω^I is called an internal boundary $\partial\Omega^I$. The elastic properties in a region Ω^I are assumed to be isotropic hyperelastic modulus in term of strain energy potential W^I. In the medium, the deformation gradient $\mathbf{F}=\mathbf{I}+\partial\mathbf{u}/\partial\mathbf{X}$ is described from the displacement $\mathbf{u}(\mathbf{X})$ in Lagrangian coordinate system and the Green strain is $\mathbf{E}=(\mathbf{F}^T\mathbf{F}-\mathbf{I})/2$. The strain energy W^I of local region Ω^I introduces the second Piola–Kirchoff stress $\mathbf{S}=\partial W^I/\partial\mathbf{E}$, which is energy conjugate to the Green strain. The governing equation and boundary conditions for finding $\mathbf{u}(\mathbf{X})$ are defined as

$$\begin{aligned} &\nabla(\mathbf{S}\cdot\mathbf{F}^T)+\mathbf{b}(\mathbf{X},\mathbf{u}(\mathbf{X}))=0 && \mathbf{X}\in\Omega \text{ or } \Omega^I \\ &(\mathbf{S}\cdot\mathbf{F}^T)\cdot\mathbf{n}=\hat{\mathbf{t}}(\mathbf{X}) && \mathbf{X}\in\partial\Omega_t \\ &\mathbf{u}(\mathbf{X})=\hat{\mathbf{u}}(\mathbf{X}) && \mathbf{X}\in\partial\Omega_d \end{aligned}, \quad (1)$$

where $\mathbf{b}$ is body force and $\mathbf{n}$ is normal on $\partial\Omega_t$. For each breathing phase, corresponding intrapleural pressure change determines distributed surface traction $\hat{\mathbf{t}}$ in quasistatic problem[49] of Eq. (1) and resultant algebraic equations of each loading step were solved by Newton iterative algorithm in ABAQUS.

It is essential to use empirically derived stress-strain constitutive relationships. Such constitutive equations of human lung tissue have been rarely reported.[55,56] Some existing models represent lung tissue as a linear elastic material.[34,37,38] However, nonlinear hyperelastic constitutive models have been presented by Zeng *et al.*[55] based on excised cadaver lung parenchyma, which is used in this study. The parameters of this model are presented in Table I.

Another important feature of physics-based lung modeling is that the motion of the lungs is asymmetric due, in part,

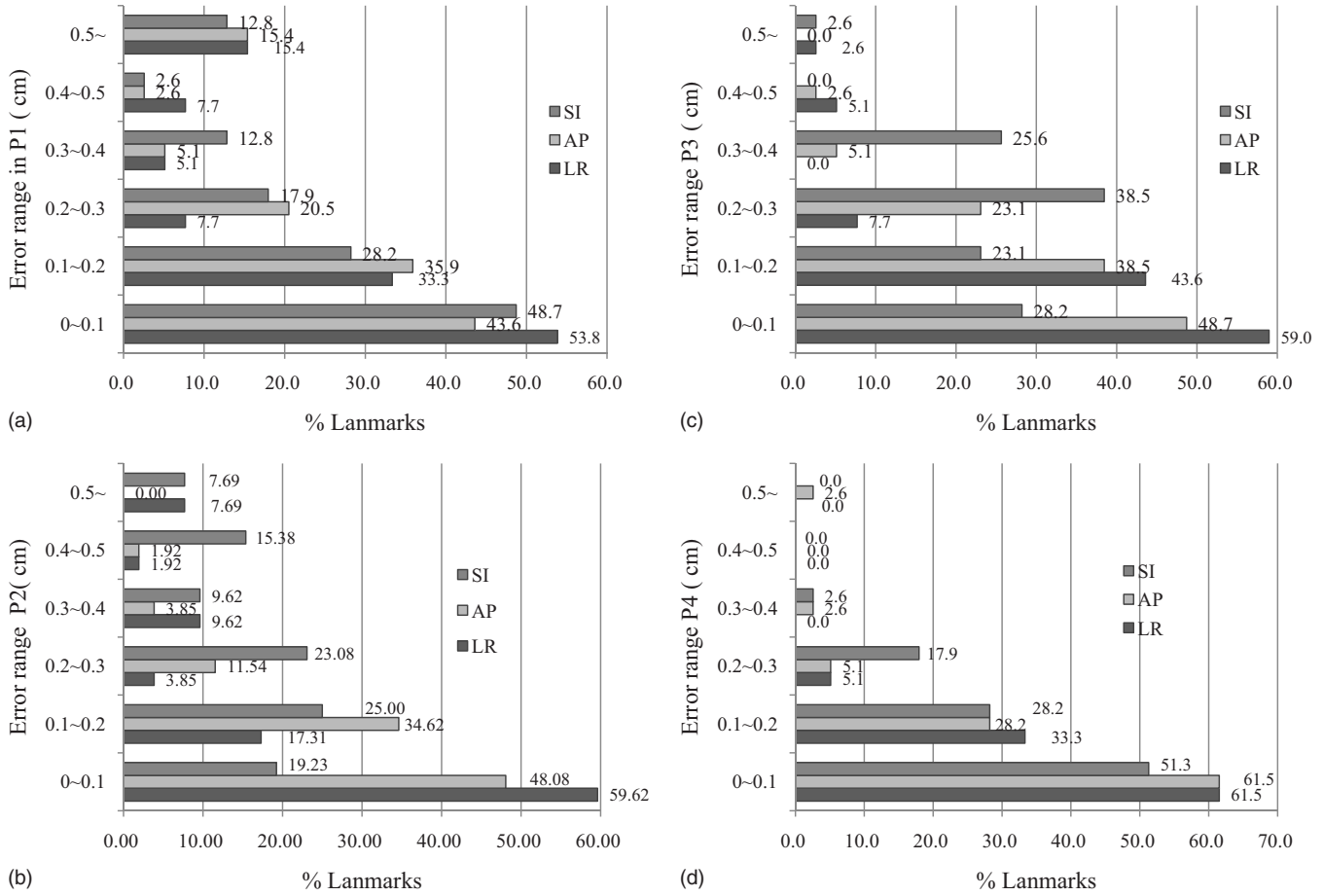

FIG. 8. Prediction errors at landmarks between EE and EI for each patient: (a) P1, (b) P2, (c) P3, and (d) P4.

TABLE V. Mean deviation of FE model prediction from 4DCT data at four different lung regions: P1–P4 (the numbers of landmarks in each region are within parentheses).

Region (number of landmark)	Mean deviation of FEM prediction at bifurcation points at EI (cm)			
	LR	AP	SI	Magnitude
	(a) Patient P1			
Whole model (48)	−0.003 ± 0.346	0.130 ± 0.271	0.013 ± 0.272	0.450 ± 0.330
Upper left(7)	−0.043 ± 0.112	0.013 ± 0.074	−0.027 ± 0.046	0.131 ± 0.058
Upper right(5)	0.134 ± 0.097	0.083 ± 0.066	−0.163 ± 0.114	0.242 ± 0.135
Lower left(16)	0.173 ± 0.352	0.172 ± 0.289	0.065 ± 0.320	0.490 ± 0.350
Lower right (20)	−0.165 ± 0.580	0.149 ± 0.326	0.030 ± 0.296	0.585 ± 0.472
	(b) Patient P2			
Whole model (48)	0.073 ± 0.221	0.066 ± 0.146	0.245 ± 0.200	0.387 ± 0.169
Upper left (15)	−0.049 ± 0.077	0.085 ± 0.119	0.257 ± 0.099	0.307 ± 0.098
Upper right (16)	0.289 ± 0.247	0.123 ± 0.118	0.347 ± 0.193	0.560 ± 0.11
Lower left (8)	−0.027 ± 0.097	−0.06 ± 0.110	0.109 ± 0.163	0.224 ± 0.098
Lower right (9)	−0.013 ± 0.116	0.044 ± 0.201	0.168 ± 0.278	0.360 ± 0.141
	(c) Patient P3			
Whole model (46)	0.024 ± 0.225	−0.093 ± 0.148	−0.190 ± 0.142	0.319 ± 0.186
Upper left (10)	−0.023 ± 0.171	−0.099 ± 0.070	−0.131 ± 0.102	0.238 ± 0.110
Upper right (15)	−0.052 ± 0.117	−0.084 ± 0.152	−0.107 ± 0.143	0.237 ± 0.141
Lower left (16)	0.164 ± 0.295	−0.103 ± 0.130	−0.276 ± 0.112	0.417 ± 0.228
Lower right (5)	−0.105 ± 0.057	−0.074 ± 0.298	−0.281 ± 0.096	0.413 ± 0.089
	(d) Patient P4			
Whole model (39)	−0.038 ± 0.103	0.036 ± 0.136	−0.038 ± 0.141	0.204 ± 0.102
Upper left (9)	−0.014 ± 0.064	0.032 ± 0.098	−0.020 ± 0.142	0.161 ± 0.082
Upper right (15)	−0.060 ± 0.134	0.091 ± 0.066	−0.104 ± 0.076	0.216 ± 0.050
Lower left (8)	0.014 ± 0.073	0.062 ± 0.077	0.044 ± 0.154	0.177 ± 0.076
Lower right (7)	−0.079 ± 0.078	−0.108 ± 0.233	−0.014 ± 0.192	0.266 ± 0.190

to the sliding of the pleural membrane on the inside of the chest wall. The surface area of the pleura that comes in contact with the chest wall is a function of deformation and cannot be determined *a priori*.[36] This introduces nonlinearities known as "contact nonlinearities."[44] Hence, we have included pleural sliding in our model. The pleural membrane can slide against the chest wall at velocities up to 20 cm/s during vigorous respiration. Lubrication is provided by a thin layer of fluid, typically 20 μm thick in the pleural space.[50] Experimental friction data between the pleura and the inner chest wall do not exist. Hence, in this paper, we have assumed frictionless contact conditions.

III. RESULTS AND DISCUSSION

III.A. Comparison of Laplacian smoothing vs NURBS surface reconstruction

To evaluate the NURBS surface reconstruction procedure tested against conventional mesh preparation using multiple Laplacian smoothing and decimating,[38,46] we compared the geometric quality of the elements. Four mesh quality indices, commonly used in computer sided engineering[49] are considered in this study.

(a) *Aspect ratio*: This is the ratio of the longest edge of an element to its shortest edge.
(b) *Maximum and minimum interior angles*: These maximum and minimum values are evaluated independently for triangle facet.
(c) *Jacobian*: The determinant of the Jacobian matrix measures the deviation of an element from its ideal or "perfect" shape, such as a triangle's deviation from equilateral. In HYPERMESH, a ratio of the maximum to the minimum value of this determinant at all the Gauss points is available for each element. A value of this ratio closer to 1.0 indicates less distortion, whereas a value closer to 0.0 signifies a highly distorted element.

In Fig. 6, elements which violate the mesh quality indices for each approach are color-coded. The results show that the threshold for violation is 0.9 for the Jacobian, 2.0 for the aspect ratio, and 80° and 50° for the maximum and minimum interior angle, respectively. The volume change indicates loss of geometric features. It is clear that the proposed geometric modeling procedure preserves initial geometry of the CT scan data. Laplacian smoothing is an algorithm to smooth a polygonal mesh. For each vertex in the mesh, a new position is chosen based on local information (such as the posi-

TABLE VI. EE-EI prediction errors between for models in the literature.

Author	Model accuracy
Didier *et al.* (2007)[a]	Average displacement error measured by landmarks is between 2.14 and 5.16 mm for different subjects
Brock *et al.* (2005)[b]	Average displacement error measured by landmarks is 4.4 mm in vector magnitude, 1.9 mm in LR, 2.8 mm in AP, and 1.7 mm in SI direction
Al-Mayah *et al.* (2008)[c]	Average displacement errors measured by landmarks
	Linear elastic model: −2.0 mm in LR, −1.0 mm in AP, and 7.1 mm in SI
	Hyperelastic model: −1.2 mm in LR, 0.0 mm in AP, and −0.3 mm in SI
	Hyperelastic/contact model: 1.4 mm in LR, 0.6 mm in AP, and 0.8 mm in SI
Al-Mayah *et al.* (2008)[d]	Average absolute error in the SI direction of hyperelastic/frictionless contact model: 2.1 mm (Poisson's ratio=0.35 and 0.4)
Werner *et al.*(2008)[e]	Displacement errors measured by landmarks at trachea bifurcation are between 2 and 7 mm

[a]Reference 39.
[b]Reference 38.
[c]Reference 35.
[d]Reference 42.
[e]Reference 34.

tion of neighbors) and then the vertex is moved. Laplacian smoothing focuses on moving point locations to improve triangulation without any guarantees on the preservation of the original geometric features.

In studies reported by Refs. 38, 41, and 10, iterations of Laplacian smoothing and additional ten smoothing iterations with decimation were used to prepare the computational mesh. Table II shows that ten cycles of smoothing iterations can reduce the original volume by 20.3 ml and the relaxing operations failed to enhance the mesh quality indices, while our proposed approach achieved higher quality meshes with 13.2 ml of volume loss.

III.B. Evaluating modeling accuracy based on landmarks for multiple patients

The procedure in this study to evaluate the modeling accuracy was based on the patient-specific models and 4DCT image data. As shown in Fig. 7, anatomical points that represent the bifurcation of vessels and airways were chosen on the exhale and inhale images. For each patient data set, 39–48 such landmarks were chosen from the 4DCT images over multiple breathing phases. For obtaining the landmarks, we followed the procedure described by Sarrut *et al.*[57] The motion patterns of these points in the 4DCT images were compared to the motion of the corresponding points in the FE model to evaluate the modeling accuracy.

Table III summarizes the details of each patient FE model. The commercial FE software package ABAQUS (Dassault Systèmes, Providence, RI) was used to simulate the model on an Intel Core2 Quadcore 2.83 GHz CPU machine with 8 GB RAM. Each computation runs till each finite-element model is subjected to the pressure loading history according to the volume change in Table IV. Due to its nonlinearity from lung tissue property and contact procedure, the computation time of each model is independent from its number of unknowns.

The model developed in this study can predict motion at multiple respiratory phases; each breathing phase is distinguished by its volume change of the segmented 4DCT data from EE (breathing phase with minimum volume) and is provided a unique identifier in Table IV.

III.C. Prediction of lung motion between EE and EI

The average of the position error and standard deviation in each direction are used as metrics of comparison in this study. If x_{4DCT} is the position of landmark in 4DCT and x_{FEM} is the position of landmark in the corresponding FEM model, then we define the prediction error as in Al-Mayah *et al.*[35]

$$\Delta x = x_{FEM} - x_{4DCT}. \quad (2)$$

Figure 8 plots a histogram of the absolute values of the prediction error between EE and EI. The average difference of end-inspiration in position between the landmarks and those predicted by the model, are observed to be 0.450 ± 0.330 cm (average $\pm$ standard deviation) for Patient P1, 0.387 ± 0.169 cm for Patient P2, 0.319 ± 0.186 cm for Patient P3, and 0.204 ± 0.102 cm for Patient P4 in the magnitude of error vector, respectively. In the lungs, the superior-inferior (SI) direction is the predominant motion direction compared to the anterior-posterior (AP) or left-right (LR). For the majority of the landmarks, the displacement errors are less than 3 mm. It should be noted that the landmarks are located at the bifurcations of vessel or airway where effects of heterogeneity of the lung tissue are significant. Also, note that all 3D CT images have slice spacing of 2 mm and that, consequently, landmark identification can induce an error of up to

TABLE VII. Mean errors of the FE model prediction from the 4DCT data at different breathing phases for (a) P1, (b) P2, (c) P3 and (d) P4.

	Mean error of FE prediction at landmark points (cm)			
Breathing phase	LR	AP	SI	Magnitude
		(a) Patient P1		
IN-1	−0.018 ± 0.257	0.007 ± 0.200	−0.012 ± 0.198	0.235 ± 0.252
IN-2	0.045 ± 0.347	0.082 ± 0.288	−0.048 ± 0.260	0.375 ± 0.320
EI	−0.003 ± 0.346	0.130 ± 0.271	0.013 ± 0.272	0.450 ± 0.330
EX-1	0.037 ± 0.435	0.270 ± 0.268	−0.111 ± 0.319	0.554 ± 0.319
EX-2	0.043 ± 0.421	0.260 ± 0.252	−0.165 ± 0.350	0.599 ± 0.268
EX-3	−0.006 ± 0.431	0.297 ± 0.246	−0.173 ± 0.313	0.613 ± 0.282
EX-4	−0.033 ± 0.372	0.215 ± 0.263	−0.142 ± 0.295	0.531 ± 0.285
		(b) Patient P2		
IN-1	−0.003 ± 0.187	0.115 ± 0.163	0.004 ± 0.239	0.333 ± 0.145
IN-2	0.028 ± 0.259	0.213 ± 0.209	0.036 ± 0.283	0.442 ± 0.201
IN-3	0.054 ± 0.246	0.114 ± 0.137	0.259 ± 0.198	0.415 ± 0.167
IN-4	0.064 ± 0.235	0.100 ± 0.130	0.260 ± 0.194	0.405 ± 0.161
EI	0.073 ± 0.221	0.066 ± 0.146	0.245 ± 0.200	0.387 ± 0.169
EX-1	−0.008 ± 0.123	0.001 ± 0.126	0.003 ± 0.230	0.230 ± 0.108
EX-2	−0.014 ± 0.102	−0.001 ± 0.123	0.007 ± 0.235	0.191 ± 0.085
		(c) Patient P3		
IN-1	−0.006 ± 0.127	0.054 ± 0.140	0.034 ± 0.104	0.199 ± 0.101
IN-2	−0.010 ± 0.157	0.112 ± 0.174	0.000 ± 0.143	0.274 ± 0.108
IN-3	0.001 ± 0.247	0.057 ± 0.195	−0.098 ± 0.185	0.318 ± 0.207
IN-4	0.016 ± 0.231	−0.018 ± 0.131	−0.188 ± 0.160	0.310 ± 0.187
IN-5	0.050 ± 0.232	−0.094 ± 0.134	−0.197 ± 0.144	0.320 ± 0.197
EI	0.024 ± 0.225	−0.093 ± 0.148	−0.190 ± 0.142	0.319 ± 0.186
EX-1	0.025 ± 0.234	−0.070 ± 0.139	−0.116 ± 0.144	0.283 ± 0.180
EX-2	0.019 ± 0.159	−0.102 ± 0.125	−0.131 ± 0.132	0.265 ± 0.122
EX-3	0.152 ± −0.014	−0.133 ± −0.062	−0.032 ± −0.038	0.205 ± 0.165
		(d) Patient P4		
IN-1	−0.034 ± 0.128	0.018 ± 0.107	−0.050 ± 0.107	0.179 ± 0.103
IN-2	−0.008 ± 0.117	0.041 ± 0.124	−0.065 ± 0.127	0.198 ± 0.106
EI	−0.038 ± 0.103	0.036 ± 0.136	−0.038 ± 0.141	0.204 ± 0.102
EX-1	−0.029 ± 0.110	0.018 ± 0.112	−0.075 ± 0.123	0.187 ± 0.105
EX-2	0.021 ± 0.171	0.002 ± 0.142	−0.035 ± 0.129	0.225 ± 0.126
EX-3	0.008 ± 0.154	−0.018 ± 0.130	0.021 ± 0.146	0.208 ± 0.134
EX-4	0.036 ± 0.137	−0.004 ± 0.150	0.064 ± 0.145	0.202 ± 0.161

2 mm in superior-inferior direction. A model predicative of 2 mm error may be used to reduce margin of the planning target volume. Although Patient P1 model had the smallest volume change in this study, complex geometric feature around the hilum prevented the pleural sliding along the AP and LR direction and brought more erroneous result at the lower right part of the lung.

Table V summarizes the prediction errors in four regions of the lungs. The lower and upper part of lung are divided at the midpoint of each lung in SI direction. It is interesting to note that there are significant regional differences in prediction error. In this table, the predictions for the lower-right regions of the lung are more accurate than the upper-right regions. These discrepancies may be caused by the assumptions in the proposed modeling method. First, the intrapleural pressure may have spatial variations on the surface of the lungs. This may be due to uneven compliance, uneven airway resistance, or the lungs sagging due to their weight. None of these effects have been considered in this model. Second, it has been reported that tumor-bearing regions have a considerably lower mobility than the corresponding tumor-free regions[13] (4.1 ± 2 vs 6.2 ± 2.5 cm). For Patient P2, we chose five landmarks around tumor as shown as Fig. 7 and the mean deviation of this tumor region is 0.041 ± 0.212 cm in LR, 0.061 ± 0.152 cm in AP, 0.515 ± 0.113 cm in SI, and 0.571 ± 0.109 cm in magnitude. This may explain the differences in left vs right and tumor-bearing vs healthy tissue in Table V. Additionally, geometric misalignment between ROIs and landmarks or the surface of EE and EI may exist during geometric modeling.

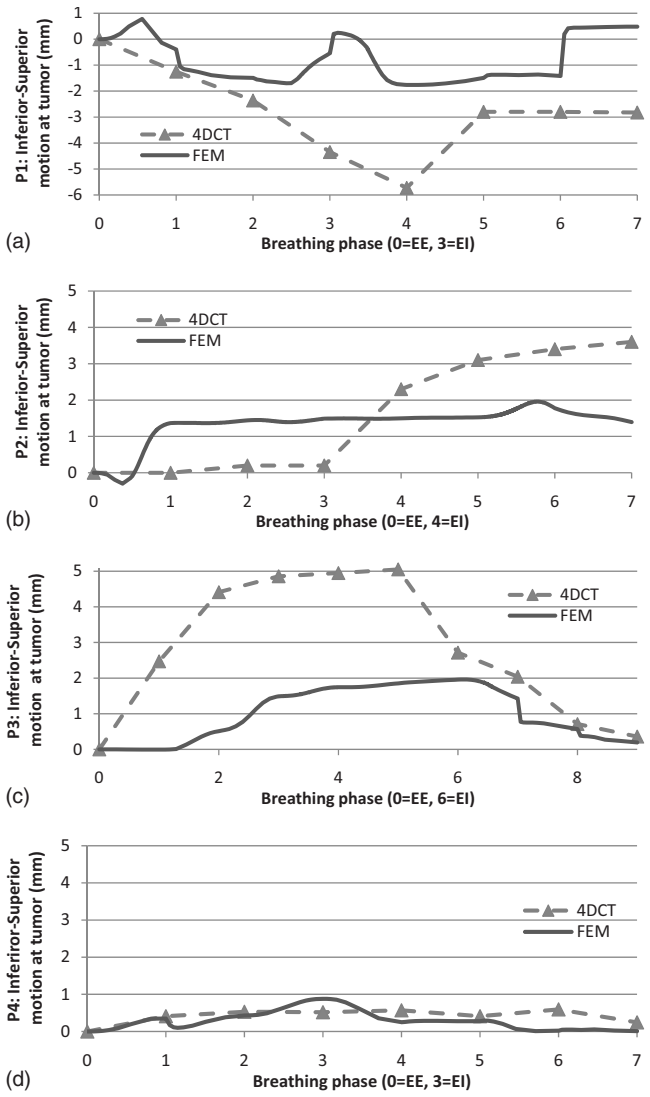

FIG. 9. Inferior-superior motion of landmark at tumor centroid for proposed model and 4DCT over multiple breathing phases: (a) P1, (b) P2, (c) P3, and (d) P4.

Table VI lists the prediction error of the previous physically based respiratory models found in the literature. As reported, parametric studies involving linear elastic parameters (Young's modulus and Poisson's ratio) have been conducted by Werner *et al.*[34] Villard *et al.*,[40] whereas a parametric study of friction coefficients has been performed in Al-Mayah *et al.*[42] However, it is noted that these parameters should have been empirically obtained in the context of biomechanics. In comparison, our model involved no tuning of FE modeling parameters including material properties,[34] contact stiffness,[37] or friction coefficients,[42] and contains the respiratory motion corresponding to the complete breathing cycle with positional accuracy better than 3 mm, on average.

III.D. Prediction of lung motion at multiple breathing phases

The mean errors, i.e., deviations of our model predictions from the landmark data at multiple breathing phases are presented in Table VII. It is noteworthy that the average error in the superior-inferior direction is less than 3 mm, which suggests that our modeling approach is consistent in accuracy over the entire breathing cycle. Contrary to previously reported studies,[58] which indicate that greater lung expansion is associated with greater prediction error, the result shows that the prediction error in the superior-inferior direction is not the greatest at EI. What may be observed from Table VII is that the prediction error does, in most cases, exhibit a cyclical behavior with the location of the peak error being determined by factors including location of the tumor and interactions of the lungs with the ribcage through pleural sliding. Deviation from this behavior may be observed in Patient P4, and the error is not cyclic possibly because the tumor of P4 is located on the pleural surface which alters its sliding response compared to other patients.

To check the temporal prediction capability of proposed mode, Fig. 9 shows that the inferior-superior motion of the landmark at tumor centroid (positive is the downward direction in figure). As shown in Sec. III C, Patient P1 has more error in the other breathing phases as in EI. In this study, we used same biomechanical properties and pressure loading history for all four patients. This may show a temporal physiological modeling factor which can address the each patient's pathological conditions such as breathing patterns and elastic property of the lesion and healthy tissue. It is noteworthy that smaller tumor motion in 4DCT gives the smaller discrepancy in the proposed FEM model in P4. Some of the major simplifying assumptions in our model include neglecting the complex alveolar structure of the lungs and modeling them as homogeneous structures, using a parameterized P-V curve[52] and assuming the tumor tissue to have the same mechanical properties as the healthy lung tissue. We show that in spite of these simplifications, the model is predictive and reasonably accurate. Prediction of tumor motion may be improved by assuming a different material model for the tumor. However, biomechanical characterization of the tumor must be performed prior to such modeling.

TABLE VIII. Mean error of linear prediction (Ref. 45) at IN-1 and EX-2 in Patient P2.

	Patient P2: Mean error of linear prediction from EE-EI at landmark points (cm)			
Breathing phase	LR	AP	SI	Magnitude
IN-1	0.030 ± 0.147	0.123 ± 0.132	0.111 ± 0.210	0.405 ± 0.130
EX-2	0.055 ± 0.233	0.220 ± 0.199	0.090 ± 0.218	0.491 ± 0.215

Most of the existing FE models report prediction of one breathing phase at EI from EE[34,35,37,39] and a linear interpolation between EE-EI is used to predict the breathing motion in the middle of EE-EI.[45] For comparison, we also perform the linear prediction[45] through interpolation between EE and EI of Patient P2 and compare the mean errors as a result of linear prediction in Table VIII at midinspiration (IN1) and midexpiration (EX2). The magnitudes of mean error of the proposed nonlinear FEM are 0.333 and 0.191 cm at IN1 and EX2, respectively, compared to 0.405 (IN1) and 0.491 cm (EX2) for the linear model predictions, indicating better accuracy.

IV. CONCLUSIONS

The primary goal of this study was to develop a method of FE modeling of the lung motion for the purposes of radiation treatment planning and dosimetry evaluation. Special attention was paid to the adoption of anatomically realistic geometry, physiologically relevant boundary conditions, pleural sliding, and nonlinear constitutive model. For geometric modeling of the lungs and ribcage, an intermediate NURBS surface between 4DCT images and meshes has been constructed for FE computation. The results show that this approach avoids multiple geometric smoothing procedures used by many researchers and is more efficient while preserving geometric features of the CT data. A P-V relationship was used to provide physiologically relevant boundary conditions to the FE model over the entire breathing cycle. Expert-based validation using landmarks from 4DCT image of four patients and FE model shows that the mean position errors between our FE model and 4DCT data are within 3 mm in SI direction over the complete respiratory cycle. Furthermore, the nonlinear FE predictions show more accurate results over full breathing cycle than linear interpolation between EE and EI.

Some of the limitations of this study include the treating the complex hierarchical alveolar structure of the lungs as homogeneous structures, using a generic P-V curve, and assuming same mechanical properties of the tumor as the healthy lung tissue. In spite of these simplifications, the study demonstrated that the FE model is predictive over the entire breathing cycle with clinically acceptable accuracy. Prediction of tumor motion may be further improved when biomechanical characterization of the tumor becomes available in the future.

Unlike previous models, the parameters of the model reported here are physiologically identifiable and measurable, so that the results can be refined by patient-specific measurement of modeling parameters and extended to other patients and additional neighboring organs affected by respiratory motion. Future studies will consider multiple organs such as the diaphragm in the simulation scenario in order to gain insight into the effects of their interactions. A nonlinear viscoeleastic model of lung tissue will need to be developed in the future to more accurately represent the energy dissipation mechanisms using new data from experimental characterization of lung tissue. Finally, the model developed here is for normal breathing. For active breathing, modifications to this model would be necessary including ribcage rotation and intercostals muscle contraction and relaxation.

ACKNOWLEDGMENTS

The authors would like to gratefully acknowledge the funding support from NIH/NLM Grant No. R01LM009362.

[a]Telephone: 518-276-4014 (will forward automatically); Fax: 518-276-4832; Electronic mail: xug2@rpi.edu; URL: http://RRMDG.rpi.edu.
[b]Author to whom correspondence should be addressed. Electronic mail: des@rpi.edu; Telephone: (518) 276-6096; Fax: (518) 276-6025 20.

[1]ICRU, "Prescribing, recording and reporting photon beam therapy (supplement to ICRU Report 50)," ICRU Report No. 62 (International Commission on Radiation Units and Measurements, Bethesda, MD, 1999).
[2]P. Keall, G. Mageras, J. Balter, R. Emery, K. Forster, S. Jiang, J. Kapatoes, D. Low, M. Murphy, and B. Murray, "The management of respiratory motion in radiation oncology report of AAPM Task Group 76," Med. Phys. **33**, 3874–3900 (2006).
[3]S. Korreman, T. Juhler-Nottrup, G. Fredberg Persson, A. Navrsted Pedersen, M. Enmark, H. Nystrom, and L. Specht, "The role of image guidance in respiratory gated radiotherapy," Acta Oncol. (Madr) **47**, 1390–1396 (2008).
[4]G. Li, D. Citrin, K. Camphausen, B. Mueller, C. Burman, B. Mychalczak, R. Miller, and Y. Song, "Advances in 4D medical imaging and 4D radiation therapy," Technol. Cancer Res. Treat. **7**, 67–81 (2008).
[5]X. Li, P. Keall, and C. Orton, "Respiratory gating for radiation therapy is not ready for prime time," Med. Phys. **34**, 867–870 (2007).
[6]M. Murphy, "Fiducial-based targeting accuracy for external-beam radiotherapy," Med. Phys. **29**, 334–344 (2002).
[7]Q. Ren, S. Nishioka, H. Shirato, and R. Berbeco, "Adaptive prediction of respiratory motion for motion compensation radiotherapy," Phys. Med. Biol. **52**, 6651–6661 (2007).
[8]D. Ruan, J. Fessler, and J. Balter, "Real-time prediction of respiratory motion based on local regression methods," Phys. Med. Biol. **52**, 7137–7152 (2007).
[9]G. Sharp, S. Jiang, S. Shimizu, and H. Shirato, "Prediction of respiratory tumour motion for real-time image-guided radiotherapy," Phys. Med. Biol. **49**, 425–440 (2004).
[10]H. Shirato, S. Shimizu, T. Kunieda, K. Kitamura, M. Van Herk, K. Kagei, T. Nishioka, S. Hashimoto, K. Fujita, and H. Aoyama, "Physical aspects of a real-time tumor-tracking system for gated radiotherapy," Int. J. Radiat. Oncol., Biol., Phys. **48**, 1187–1195 (2000).
[11]S. Webb, "Motion effects in (intensity modulated) radiation therapy: A review," Phys. Med. Biol. **51**, R403–R425 (2006).
[12]L. Xing, B. Thorndyke, E. Schreibmann, Y. Yang, T.-F. Li, G.-Y. Kim, G. Luxton, and A. Koong, "Overview of image-guided radiation therapy," Med. Dosim. **31**, 91–112 (2006).
[13]C. Plathow, S. Ley, C. Fink, M. Puderbach, W. Hosch, A. Schmähl, J. Debus, and H. Kauczor, "Analysis of intrathoracic tumor mobility during whole breathing cycle by dynamic MRI," Int. J. Radiat. Oncol., Biol., Phys. **59**, 952–959 (2004).
[14]T. Bortfeld, S. B. Jiang, and E. Rietzel, "Effects of motion on the total dose distribution," Semin. Radiat. Oncol. **14**, 41–51 (2004).
[15]R. Colgan, J. McClelland, D. McQuaid, P. M. Evans, D. Hawkes, J. Brock, D. Landau, and S. Webb, "Planning lung radiotherapy using 4D CT data and a motion model," Phys. Med. Biol. **53**, 5815–5830 (2008).
[16]L. Ekberg, O. Holmberg, L. Wittgren, G. Bjelkengren, and T. Landberg, "What margins should be added to the clinical target volume in radiotherapy treatment planning for lung cancer?," Radiother. Oncol. **48**, 71–77 (1998).
[17]S. C. Erridge, Y. Seppenwoolde, S. H. Muller, M. van Herk, K. De Jaeger, J. S. A. Belderbos, L. J. Boersma, and J. V. Lebesque, "Portal imaging to assess set-up errors, tumor motion and tumor shrinkage during conformal radiotherapy of non-small cell lung cancer," Radiother. Oncol. **66**, 75–85 (2003).
[18]E. Ford, G. Mageras, E. Yorke, and C. Ling, "Respiration-correlated spiral CT: A method of measuring respiratory-induced anatomic motion for radiation treatment planning," Med. Phys. **30**, 88–97 (2003).

[19]S. Vedam, P. Keall, V. Kini, H. Mostafavi, H. Shukla, and R. Mohan, "Acquiring a four-dimensional computed tomography dataset using an external respiratory signal," Phys. Med. Biol. **48**, 45–62 (2003).
[20]D. Low, M. Nystrom, E. Kalinin, P. Parikh, J. Dempsey, J. Bradley, S. Mutic, S. Wahab, T. Islam, and G. Christensen, "A method for the reconstruction of four-dimensional synchronized CT scans acquired during free breathing," Med. Phys. **30**, 1254–1263 (2003).
[21]P. Keall, S. Joshi, S. Vedam, J. Siebers, V. Kini, and R. Mohan, "Four-dimensional radiotherapy planning for DMLC-based respiratory motion tracking," Med. Phys. **32**, 942–951 (2005).
[22]J. Sonke, L. Zijp, P. Remeijer, and M. van Herk, "Respiratory correlated cone beam CT," Med. Phys. **32**, 1176–1186 (2005).
[23]S. Nehmeh, Y. Erdi, T. Pan, A. Pevsner, K. Rosenzweig, E. Yorke, G. Mageras, H. Schoder, P. Vernon, and O. Squire, "Four-dimensional (4D) PET/CT imaging of the thorax," Med. Phys. **31**, 3179–3186 (2004).
[24]A. Krogh, *The Comparative Physiology of Respiratory Mechanisms* (University of Pennsylvania Press, Philadelphia, 1941).
[25]M. J. Murphy and D. Pokhrel, "Optimization of an adaptive neural network to predict breathing," Med. Phys. **36**, 40–47 (2009).
[26]M. Murphy and S. Dieterich, "Comparative performance of linear and nonlinear neural networks to predict irregular breathing," Phys. Med. Biol. **51**, 5903–5914 (2006).
[27]B. Suki, S. Ito, D. Stamenovic, K. R. Lutchen, and E. P. Ingenito, "Biomechanics of the lung parenchyma: Critical roles of collagen and mechanical forces," J. Appl. Physiol. **98**, 1892–1899 (2005).
[28]G. Holzapfel, "Biomechanics of soft tissue," in *The Handbook of Materials Behavior Models* (Academic Press, San Diego, 2001), Vol. 3, pp. 1049–1063.
[29]S. Loring, R. Brown, A. Gouldstone, and J. Butler, "Lubrication regimes in mesothelial sliding," J. Biomech. **38**, 2390–2396 (2005).
[30]E. D'Angelo, S. Loring, M. Gioia, M. Pecchiari, and C. Moscheni, "Friction and lubrication of pleural tissues," Respir. Physiol. Neurobiol. **142**, 55–68 (2004).
[31]J. M. Guccione, K. D. Costa, and A. D. McCulloch, "Finite element stress analysis of left ventricular mechanics in the beating dog heart," J. Biomech. **28**, 1167–1177 (1995).
[32]Y. Seppenwoolde, H. Shirato, K. Kitamura, S. Shimizu, M. van Herk, J. Lebesque, and K. Miyasaka, "Precise and real-time measurement of 3D tumor motion in lung due to breathing and heartbeat, measured during radiotherapy," Int. J. Radiat. Oncol., Biol., Phys. **53**, 822–834 (2002).
[33]D. Yang, W. Lu, D. Low, J. Deasy, A. Hope, and I. El Naqa, "4D-CT motion estimation using deformable image registration and 5D respiratory motion modeling," Med. Phys. **35**, 4577–4590 (2008).
[34]R. Werner, J. Ehrhardt, R. Schmidt, and H. Handels, "Modeling respiratory lung motion: A biophysical approach using finite element methods," Proc. SPIE **6916**, 69160N (2008).
[35]A. Al-Mayah, J. Moseley, and K. Brock, "Contact surface and material nonlinearity modeling of human lungs," Phys. Med. Biol. **53**, 305–317 (2008).
[36]J. West and F. Matthews, "Stresses, strains, and surface pressures in the lung caused by its weight," J. Appl. Physiol. **32**, 332–345 (1972).
[37]T. Zhang, N. P. Orton, T. R. Mackie, and B. R. Paliwal, "Technical note: A novel boundary condition using contact elements for finite element deformable image registration," Med. Phys. **31**, 2412–2415 (2004).
[38]K. Brock, M. Sharpe, L. Dawson, S. Kim, and D. Jaffray, "Accuracy of finite element model-based multi-organ deformable image registration," Med. Phys. **32**, 1647–1659 (2005).
[39]A. Didier, P. Villard, J. Bayle, M. Beuve, B. Shariat, H. Pradel, and F. Lyon, "Breathing thorax simulation based on pleura physiology and rib kinematics," in Proceedings of the International Conference on Medical Information Visualisation-BioMedical Visualisation, 2007, pp. 35–42.
[40]P. Villard, M. Beuve, B. Shariat, V. Baudet, and F. Jaillet, "Simulation of lung behaviour with finite elements: Influence of bio-mechanical parameters," in Proceedings of the Third International Conference on Medical Information Visualisation-Biomedical Visualisation (MediVis 2005), 2005, pp. 9–14.
[41]P. Villard, M. Beuve, B. Shariat, V. Baudet, and F. Jaillet, "Lung mesh generation to simulate breathing motion with a finite element method," in Proceedings of the Eighth International Conference on Information Visualisation, 2004, pp. 194–199.
[42]A. Al-Mayah, J. Moseley, M. Velec, and K. Brock, "Effect of friction and material compressibility on deformable modeling of human lung," in *Biomedical Simulation*, Lecture Notes in Computer Science (Springer, Berlin, 2008), pp. 98–106.
[43]F. Matthews and J. West, "Finite element displacement analysis of a lung," J. Biomech. **5**, 591–600 (1972).
[44]E. Radford, *Tissue Elasticity* (American Physiological Society, Washington, D.C., 1957), pp. 177–190.
[45]R. Werner, J. Ehrhardt, R. Schmidt, and H. Handels, "Patient-specific finite element modeling of respiratory lung motion using 4D CT image data," Med. Phys. **36**, 1500–1511 (2009).
[46]T. Nguyen, J. Moseley, L. Dawson, D. Jaffray, and K. Brock, "Adapting liver motion models using a navigator channel technique," Med. Phys. **36**, 1061–1073 (2009).
[47]J. Vandemeulebroucke, D. Sarrut, and P. Clarysse, "Point-validated pixel-based breathing thorax model," in Proceedings of the International Conference on the Use of Computers in Radiation Therapy (ICCR), 2007.
[48]L. Lin, C. T. Shi, Y. Liu, G. Swanson, and N. Papanikolaou, "Development of a novel post-processing treatment planning platform for 4D radiotherapy," Technol. Cancer Res. Treat. **7**, 125–132 (2008).
[49]K. Bathe, *Finite Element Procedures* (Prentice Hall, Englewood Cliffs, 1996).
[50]S. Lai-Fook, "Pleural mechanics and fluid exchange," Physiol. Rev. **84**, 385–410 (2004).
[51]J. West, *Respiratory Physiology: The Essentials*, 7th ed. (Williams and Wilkins, Baltimore, 2007).
[52]A. Santhanam, C. Imielinska, P. Davenport, P. Kupelian, and J. Rolland, "Modeling real-time 3-D lung deformations for medical visualization," IEEE Trans. Inf. Technol. Biomed. **12**, 257–270 (2008).
[53]E. Salazar and J. H. Knowles, "An analysis of pressure-volume characteristics of the lungs," J. Appl. Physiol. **19**, 97–104 (1964).
[54]ABAQUS, *ABAQUS Analysis: User's Manual* (Dassault Systemes, 2007).
[55]Y. Zeng, D. Yager, and Y. Fung, "Measurement of the mechanical properties of the human lung tissue," J. Biomech. Eng. **109**, 169–174 (1987).
[56]J. Gao, W. Huang, and R. Yen, "Mechanical properties of human lung parenchyma," Biomed. Sci. Instrum. **42**, 172–180 (2006).
[57]D. Sarrut, V. Boldea, S. Miguet, and C. Ginestet, "Simulation of four-dimensional CT images from deformable registration between inhale and exhale breath-hold CT scans," Med. Phys. **33**, 605–617 (2006).
[58]D. Sarrut, S. Delhay, P. Villard, V. Boldea, M. Beuve, and P. Clarysse, "A comparison framework for breathing motion estimation methods from 4-D imaging," IEEE Trans. Med. Imaging **26**, 1636–1648 (2007).